Strained endotaxial nanostructures with high thermoelectric figure of merit

Kanishka Biswas[1], Jiaqing He[1,2], Qichun Zhang[1], Guoyu Wang[3], Ctirad Uher[3], Vinayak P. Dravid[2] and Mercouri G. Kanatzidis[1,4]*

Thermoelectric materials can directly generate electrical power from waste heat but the challenge is in designing efficient, stable and inexpensive systems. Nanostructuring in bulk materials dramatically reduces the thermal conductivity but simultaneously increases the charge carrier scattering, which has a detrimental effect on the carrier mobility. We have experimentally achieved concurrent phonon blocking and charge transmitting via the endotaxial placement of nanocrystals in a thermoelectric material host. Endotaxially arranged SrTe nanocrystals at concentrations as low as 2% were incorporated in a PbTe matrix doped with Na_2Te. This effectively inhibits the heat flow in the system but does not affect the hole mobility, allowing a large power factor to be achieved. The crystallographic alignment of SrTe and PbTe lattices decouples phonon and electron transport and this allows the system to reach a thermoelectric figure of merit of 1.7 at $\sim$800 K.

Thermoelectric materials are able to directly and reversibly convert heat energy into electrical power and may have a significant impact on power generation and cooling. An efficient thermoelectric material must exhibit a high thermoelectric figure of merit, ZT, at the temperature of operation, T. The figure of merit is defined as: $ZT = (S^2\sigma/\kappa)T$, where S is the Seebeck coefficient, σ is the electrical conductivity and κ is the thermal conductivity[1,2]. Typically, there are two ways to improve the ZT of thermoelectric materials: one is to enhance the power factor (σS^2) and the other is to lower the thermal conductivity[3,4]. Approaches to increase the power factor include introducing a resonance level in the valence band—for example, in Tl–PbTe (refs 5,6)—or synergistic nanostructuring[7]. Nanoscale inclusions in bulk materials can dramatically suppress the lattice thermal conductivity by scattering the longer wavelength heat-carrying phonons, as in $AgPb_mSbTe_{m+2}$ (refs 8–10), $AgPb_mSn_nSbTe_{2+m+n}$ (ref. 11), $NaPb_mSbTe_{2+m}$ (ref. 12), PbTe–PbS (ref. 13) and BiSbTe (ref. 14). In all these cases, however, the power factor is also reduced because the nanoinclusions increase carrier scattering, which in turn adversely affects the carrier mobilities. Epitaxial superlattice thin films of Bi_2Te_3/Sb_2Te_3 were reported to exhibit a very high ZT of $\sim$2.4 at room temperature[15]. These structures use the acoustic mismatch between the superlattice components to reduce the lattice thermal conductivity, rather than using alloy scattering of carriers. Band offsets in the superlattices are chosen to allow carrier transmission. Another approach for achieving very low lattice thermal conductivities without a deterioration in electronic performance is the 'photo glass electron crystal' idea proposed by Slack[16].

Here we report that by coherently embedding SrTe nanocrystals in a bulk PbTe matrix—where the rocksalt SrTe and PbTe lattices are completely aligned (endotaxy)—at an optimum molar concentration of only 2%, heat-carrying phonons can be strongly scattered without affecting charge transport. This is the first example of a bulk thermoelectric system containing dispersed nanocrystals in which carrier scattering is impervious to the nanostructuring. The highest ZT value achieved is 1.7 at 815 K, which outperforms any reported p-type system.

To our knowledge, thermoelectric properties of the PbTe–SrTe system have not been investigated previously. Scanning transmission electron microscopy (STEM) and transmission electron microscopy (TEM) demonstrate the presence of endotaxially coherent nanostructures in the PbTe–SrTe samples. We show that this is the principal factor for the very low thermal conductivity observed. Hall coefficient measurements suggest that there is no significant hole scattering from the SrTe nanocrystals compared with pure, p-type PbTe material. The presence of the so-called second valence band[17] in PbTe becomes dominant above $\sim$450 K and it contributes significantly to achieving a high power factor.

Results and discussion

We have investigated the structural, charge transport and thermal transport properties of PbTe–SrTe (SrTe = 0.5–2 mol%) doped with 1 mol% Na_2Te. Powder X-ray diffraction patterns (Supplementary Fig. S1) of the PbTe–SrTe samples could be indexed on the PbTe structure with an $Fm\overline{3}m$ space group; no SrTe or other phase was observed within the detectability limits of X-ray diffraction. The lattice parameters expand from 6.4445(4) to 6.4606(4) Å with the increase in SrTe concentration from 0 to 2%. Overall, at low magnification, energy dispersive spectroscopy agrees with the nominal composition. Thermogravimetric analysis (not shown) shows that the samples are thermally stable up to 900 K with no measurable mass loss.

Figure 1a shows the temperature-dependent electrical conductivity, σ, of PbTe–SrTe samples doped with 1% Na_2Te and a control sample with no SrTe component. For all the samples, σ decreases with increasing temperature, indicating degenerate conduction for the entire measurement range. There is very little effect on σ with varying SrTe concentration. For the 2% SrTe sample $\sigma \approx 2,530$ S cm^{-1} at room temperature, decreasing to $\sim$240 S cm^{-1} at 800 K (Fig. 1a). The temperature-dependent electrical conductivity data for samples containing 0.5, 1 and 2% SrTe follow a power law, $\sigma \approx T^{-\delta}$ where $\delta = 2.8$, 2.7 and 2.4, respectively.

[1]Department of Chemistry, Northwestern University, Evanston, Illinois 60208, USA, [2]Department of Materials Science and Engineering, Northwestern University, Evanston, Illinois 60208, USA, [3]Department of Physics, University of Michigan, Ann Arbor, Michigan 48109, USA, [4]Materials Science Division, Argonne National Laboratory, Argonne, Illinois 60439, USA. *e-mail: m-kanatzidis@northwestern.edu
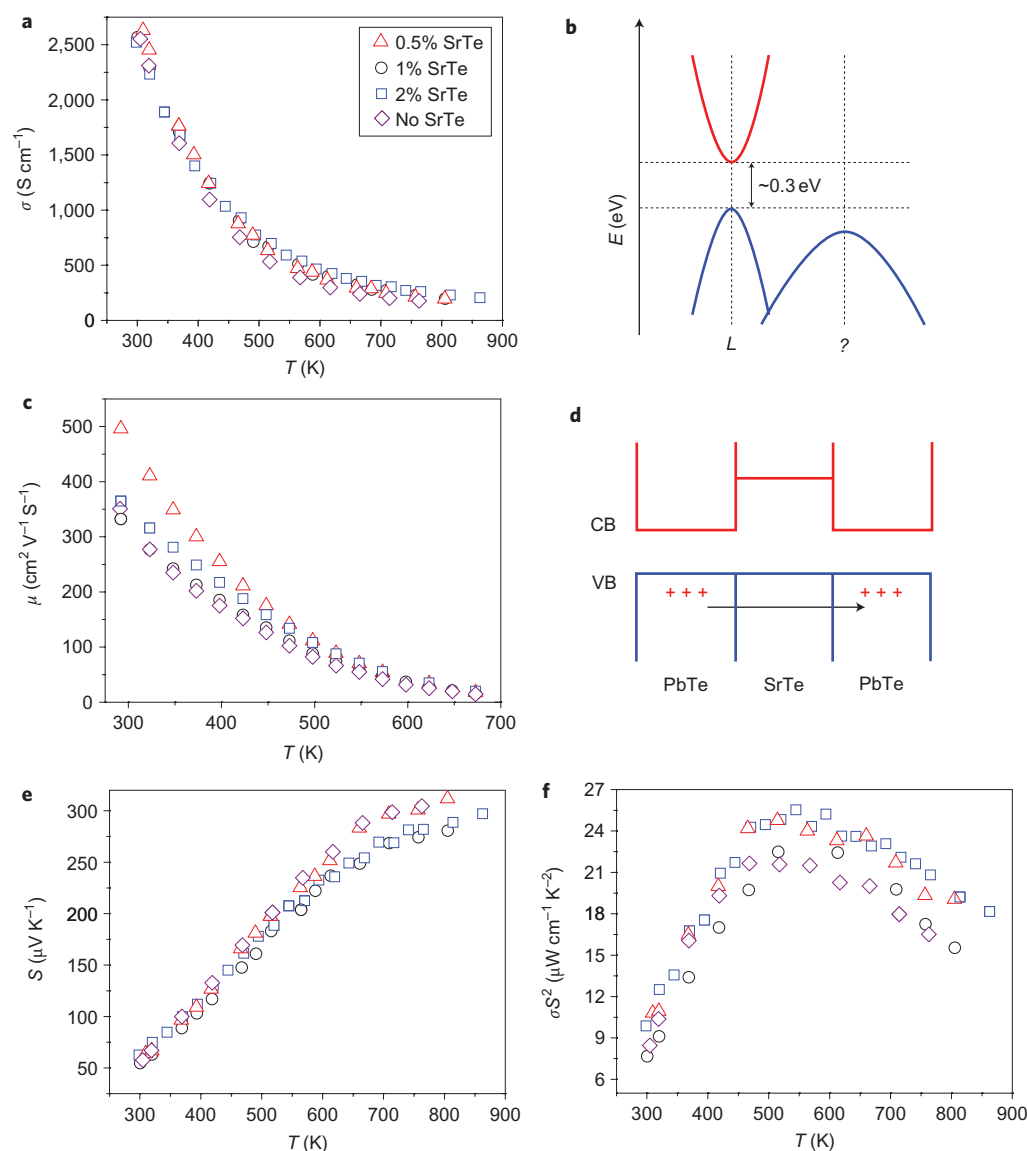
Figure 1 | Electrical transport properties of PbTe–SrTe. a, Temperature dependence of electrical conductivity (σ) of different PbTe–SrTe samples doped with 1% Na$_2$Te and a control sample containing no SrTe. The same symbol notation for the samples is used in all parts of this figure. **b**, Schematic representation of the electronic band structure energy diagram of PbTe at room temperature, highlighting the presence of a second valence band at Σ. At $T > 300$ K the second valence band significantly rises in energy. **c**, Hole mobilities of PbTe–SrTe samples doped with 1% Na$_2$Te and a control sample containing no SrTe. **d**, Schematic representation of the alignment of the valence band (VB) and conduction band (CB) energies of SrTe precipitates in the PbTe matrix at $T > 300$ K. **e,f**, Temperature-dependent Seebeck coefficient (S) (**e**) and power factor (σS^2) (**f**) of PbTe–SrTe samples doped with 1% Na$_2$Te and a control sample containing no SrTe.

The Hall coefficients, R_H, in the temperature range 300–700 K for PbTe–SrTe samples doped with 1% Na$_2$Te are positive and indicate p-type conduction (Supplementary Fig. S2a). R_H gradually increases, reaching a maximum at ~430 K, and then decreases. The position of the maximum is almost independent of the amount of SrTe. This can be explained by the two-valence-band model (light-hole and heavy-hole valence bands) of PbTe (Fig. 1b)[17–20]. The energy difference between these two valence band maxima changes with increasing temperature. The increase in R_H above 300 K occurs because carriers begin to transfer from the first (light-hole) to the second (heavy-hole) valence band. At about 450 K, the edges of the two valence bands are at approximately the same energy level and at temperatures above 450 K the main contribution to the transport comes from the heavy-hole valence band. Assuming parabolic bands and a single-band conduction process, we estimate the carrier concentration, n, to be

~5.4×10^{19} holes cm^{-3} ($n = 1/eR_H$, where e is the electronic charge) at room temperature for a sample containing 1% SrTe. Temperature-dependent carrier concentrations up to 450 K for PbTe–SrTe samples doped with 1% Na$_2$Te are given in Supplementary Fig. S2b. The Hall mobility at room temperature, defined as $\mu = \sigma/ne$, is ~340 cm^2 V^{-1} s^{-1} for samples containing 1% SrTe (Fig. 1c). For a control—p-type PbTe doped with 1% Na$_2$Te, which has a similar carrier concentration of ~5.6×10^{19} cm^{-3}—the Hall mobility at room temperature was measured to be ~350 cm^2 V^{-1} s^{-1} (Fig. 1c). The insertion of endotaxial SrTe nanocrystals in the PbTe matrix therefore does not appear to affect the hole scattering. The reason for this is two-fold: (1) three dimensional crystallographic alignment of SrTe and PbTe phases with coherent/semi-coherent interfaces; and (2) the alignment of the energies of the two valence bands in the two materials where the band offset is very small at

161

>300 K, which allows carrier transmission between two endotaxial components (Fig. 1d)[15].

First principles electronic band structure calculations on SrTe–PbTe composite structures indicate that at 0 K the band offset is only 0.17 eV with the valence band maximum of PbTe lying lower than that of SrTe. At temperatures above 300 K, the small band offset between the two phases decreases even further because there is an anomalous increase in the energy of the valence band maximum of PbTe (ref. 18) while that of SrTe is expected to decrease in energy because of lattice expansion[21]. As the valence band offset between the nanocrystal and the matrix material diminishes with rising temperature, transport across the two phases is possible with little extra scattering, as is suggested by the mobility data above.

Temperature-dependent hole mobility data for several PbTe–SrTe samples doped with 1% Na_2Te and a control PbTe sample doped with 1% Na_2Te are presented in Fig. 1c for comparison. A change in the hole mobility with temperature is observed (see log–log plot for μ versus T in Supplementary Fig. S2c) around 450 K, which indicates the involvement of the heavy-hole valence band. The carrier mobility data up to 450 K for samples containing 0.5, 1 and 2% SrTe follow the temperature-dependent power law $\mu \approx T^{-\delta}$, with $\delta = 2.4$, 2.1 and 1.9, respectively. For pure p-type PbTe, the canonical power law dependence of the mobility has an exponent δ close to 2.5 (ref. 18). The slower rate of decrease in mobility with increasing SrTe concentration indicates the reduced scattering of the hole carriers in this system and this is critical in achieving a comparatively enhanced power factor at high temperature. This is the first example of a bulk system where carrier scattering is reduced rather than increased with the introduction of a second phase in a thermoelectric semiconductor. This observation has important implications for increasing the ZT in these materials.

Figure 1e presents the Seebeck coefficient, S, as a function of temperature for PbTe–SrTe samples doped with 1% Na_2Te and a control PbTe sample doped with 1% Na_2Te. The thermoelectric power response is positive in agreement with the Hall measurements for a p-type PbTe. The highest room-temperature thermopower value measured was ~65 µV K^{-1} for the sample containing 0.5% SrTe, increasing to ~312 µV K^{-1} at ~800 K. Assuming a two-valence-band model of PbTe (Fig. 1b), the total Seebeck coefficient can be written as $S = [S_{h1}\sigma_{h1} + S_{h2}\sigma_{h2}]/\sigma$ where S_{h1} is the thermopower for light holes and S_{h2} is the thermopower for heavy holes[22,23]. At temperatures above 450 K, the main contribution to the total thermopower is made by the heavy-hole valence band, which is key to achieving a high power factor. The effective hole mass in the second valence (heavy-hole) band is 1.5 times the effective mass of light holes[18]. In the case of degenerate semiconductors the Seebeck coefficient is dependent on the effective mass of the carriers[3]. Thus, the large value of thermopower at high temperatures in a p-type PbTe–SrTe system can be explained by the contribution of the heavy-hole valence band.

Figure 1f shows the power factor, σS^2, as a function of temperature for PbTe–SrTe samples doped with 1% Na_2Te and a control PbTe sample doped with 1% Na_2Te. The highest room temperature power factor value measured was ~11 µW cm^{-1} K^{-2} for the sample containing 2% SrTe, which rises to a maximum (~25 µW cm^{-1} K^{-2}) at about 560 K and yields a value of ~20 µW cm^{-1} K^{-2} at ~800 K.

The thermal conductivity, κ_{total}, values for PbTe–SrTe samples as a function of temperature are shown in Fig. 2a. The lowest room temperature κ_{total} of ~3 W m^{-1} K^{-1} was observed for samples containing 2% SrTe. This value decreased to 0.9 W m^{-1} K^{-1} at ~800 K. The lattice thermal conductivity, κ_{lat}, was obtained by subtracting the electronic component, κ_e (κ_e can be calculated using the Wiedemann–Franz law, $\kappa_e = L\sigma T$, assuming the Lorenz number, $L_o = 2.44 \times 10^{-8}$ WΩK^{-2} corresponding to a degenerate system),
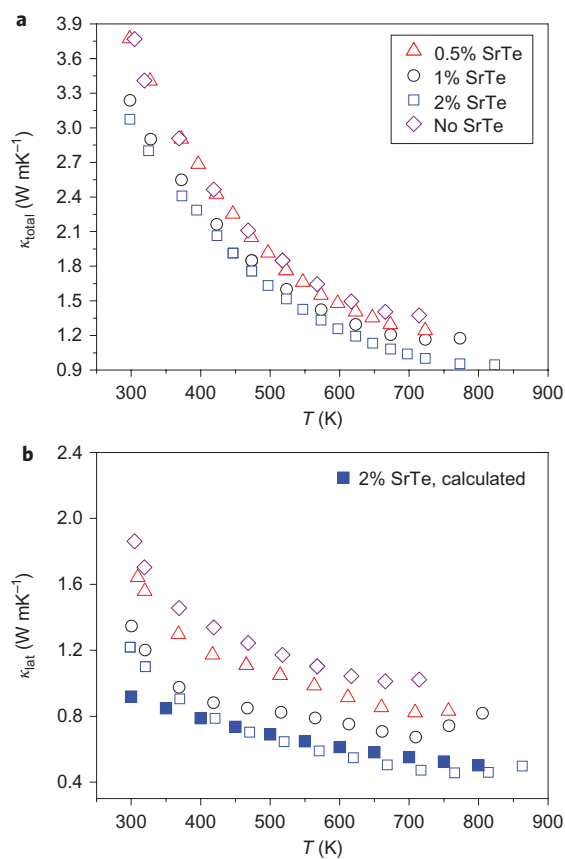

Figure 2 | Thermal transport properties of PbTe–SrTe. a,b, Temperature dependence of total thermal conductivity (κ_{total}) (**a**) and lattice thermal conductivity (κ_{lat}) (**b**) of PbTe–SrTe samples doped with 1% Na_2Te and a control sample containing no SrTe. The solid blue squares in **b** show the temperature-dependent lattice thermal conductivity calculated with the Callaway model and input parameters obtained from TEM investigation of PbTe containing 2% SrTe and 1% Na_2Te.

from κ_{total}. Figure 2b shows the temperature-dependent κ_{lat} for 0.5, 1 and 2% SrTe-containing PbTe and a control p-type sample of pure PbTe for comparison. The 2% SrTe sample exhibits the lowest room temperature κ_{lat} of ~1.2 W mK^{-1}, which at ~800 K drops to the very low value of ~0.45 W mK^{-1}. This value is only about 45% of that of pure PbTe (Fig. 2b). It is clear that a large decrease in lattice thermal conductivity occurs with insertion of SrTe in PbTe.

TEM and STEM investigations of the PbTe–SrTe samples doped with 1% Na_2Te show the presence of nanoscale precipitates with the lowest nanoparticle density observed in samples containing 0.5% SrTe and the highest in samples containing 2% SrTe. Most of the precipitates in all samples have spherical or ellipsoidal shapes. As elaborated below (and in Supplementary Information), smaller precipitates (~2–5 nm) are typically coherently strained (that is, they demonstrate elastic accommodation of an interfacial misfit), whereas larger precipitates exhibit interfacial misfit dislocations due to excess coherency strain, consistent with a small lattice parameter misfit.

In Figure 3a,b, we show typical low magnification TEM images of the 1% and 2% SrTe-containing samples. Both images show numerous regular precipitates with dark (diffraction) contrast in the range of 5–15 nm. From the single-electron diffraction pattern shown in the inset of Fig. 3b we can conclude that the PbTe matrix and SrTe nanocrystals have similar symmetry, structure and lattice parameters, and corresponding crystallographic planes and directions are completely aligned in three dimensions. Indeed, PbTe and SrTe, have similar bulk lattice parameters of 6.453 and 6.660 Å,
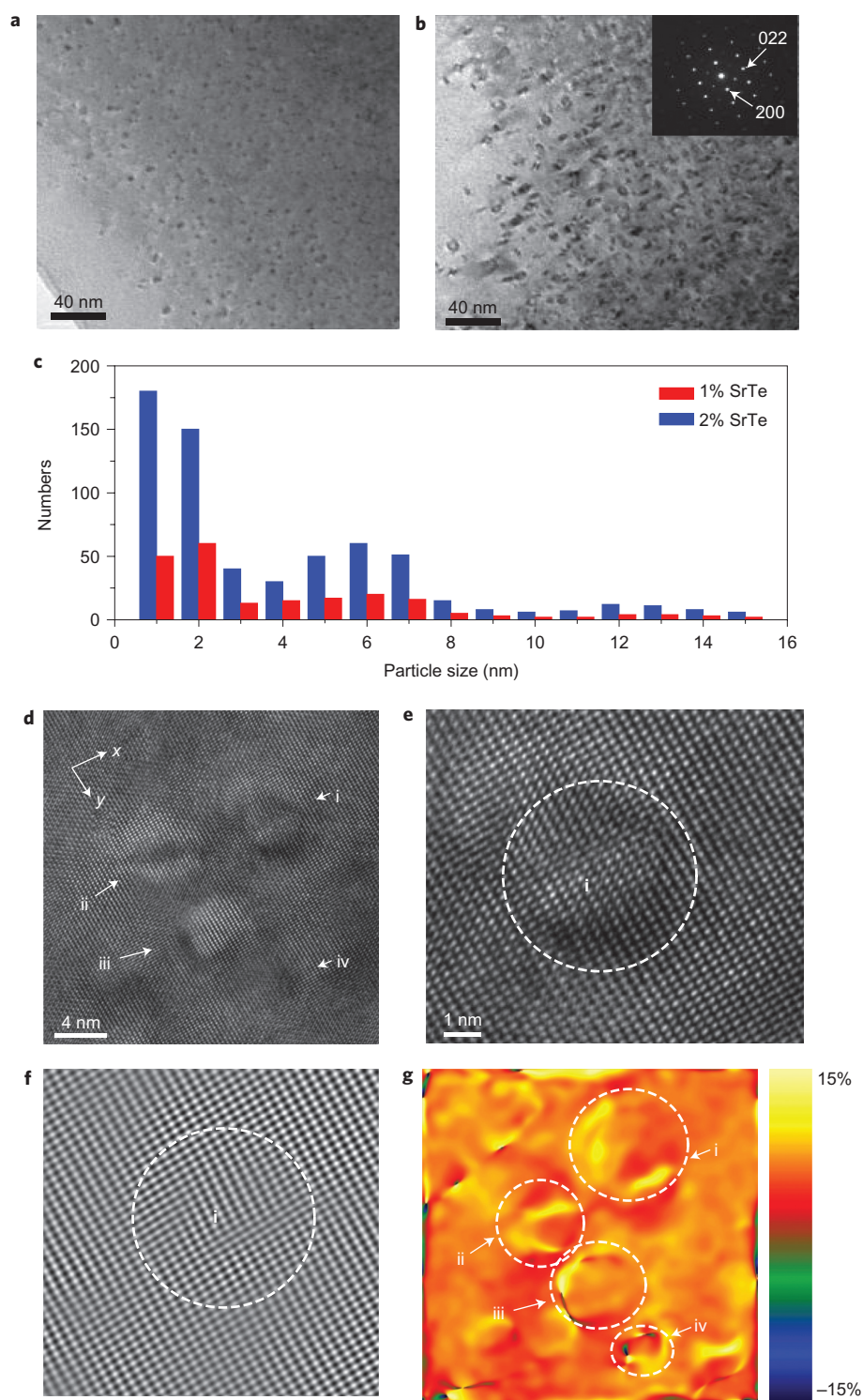
Figure 3 | TEM and strain analysis of PbTe–SrTe. a,b, Low-magnification TEM images of PbTe containing 1% SrTe (**a**) and 2% SrTe (**b**) (both doped with 1% Na_2Te). The inset in **b** shows the corresponding electron diffraction pattern, which confirms the crystallographic alignment of SrTe and PbTe lattices. **c,** SrTe nanocrystal size distribution histogram. **d,** High-resolution TEM phase contrast image of several endotaxial nanocrystals of SrTe in the PbTe matrix. **e,** Enlarged image of particle i, depicting a coherent (with elastic strain) boundary between precipitate and matrix. **f,** Inverse first Fourier transform image showing the coherent interface with no misfit dislocations. **g,** The shear strain distribution of the nanoscale inclusions showing elastic strains at and around all precipitates and the presence of plastic strain at and around dislocation cores in precipitates iii and iv. The color bar indicates 15 to –15% strain.

respectively[24]. Therefore, the SrTe nanocrystals are endotaxially placed in the PbTe matrix. Furthermore, STEM investigations (Supplementary Fig. S3a-b) show a high density of numerous small precipitates (∼1–2 nm). Although it is difficult to quantitatively determine the compositions of individual precipitates owing to their overlap with the matrix, energy dispersion X-ray spectroscopy indicates an increase in the Sr signal from the precipitates (dark areas in the STEM image) compared with the matrix regions (Supplementary Fig. S3c). The presence of SrTe nanoscale precipitates in the PbTe matrix was also confirmed by additional TEM

analyses of two control samples—PbTe with 2% SrTe but no Na$_2$Te and PbTe with 1% Na$_2$Te but no SrTe. Unfortunately, the phase diagram is unknown for a PbTe–SrTe system so it is not possible to offer a thermodynamic explanation for the formation of SrTe nanocrystals in a PbTe matrix at this moment. The TEM studies reveal that the precipitate number densities in PbTe with 2% SrTe and in PbTe with 2% SrTe and 1% Na$_2$Te are quite similar whereas the Sr-free PbTe–Na$_2$Te sample contains very few detectable precipitates. Figure 3c shows the size distribution histogram of SrTe nanocrystals for samples containing 1% and 2% SrTe under the same TEM observation volume. It is clear that the 2% SrTe sample has approximately double the precipitate density of the 1% SrTe sample. On average, the estimates of the distribution density of all types of nanoscale precipitates are all ~1.5×10^{12} cm^{-2} for PbTe with 2% SrTe and 1% Na$_2$Te. Although the SrTe precipitates have a size distribution of ~1–15 nm, for simplicity we will use an average particle size of 2 nm for our calculation of the lattice thermal conductivity.

In order to analyse the defects or strain distribution at the boundaries between the precipitates and the PbTe matrix, we performed high-resolution TEM investigations on a PbTe sample containing 2% SrTe and 1% Na$_2$Te. Figure 3d shows a typical phase contrast high-resolution TEM image containing lattice fringes of several 2–4 nm precipitates with a typical interfacial boundary (~1 nm dark contrast) between the matrix and the precipitate. Figure 3e is the enlarged high-resolution TEM image of precipitate i, which clearly shows no dislocations at the boundary marked by a dotted line. In Figure 3f, the inverse first Fourier transform reconstructed image of the precipitate also depicts a coherent (elastically strained) interface between the precipitate and matrix. To analyse the presence of elastic and plastic strain, the image in Fig. 3d was subjected to geometric phase-analysis[25], which is a lattice image processing method for semi-quantitative spatially distributed strain field analysis. Geometric phase analysis was used to investigate the variation in the lattice parameter and thus the strain at and around boundaries. To reduce the potential artifacts of the strain analysis, it is necessary to obtain high quality, clear lattice images. Figure 3g shows the shear strain map profiles (ε_{xy}) of the precipitates. From the strain map distribution in this image, it appears that elastic strain is pervasive in and around all precipitates, although there is additional plastic strain around the dislocation cores in particles iii and iv. We can also see that the dark contrast in Fig. 3d is not identical to the strain region in Fig. 3e. This is due to diffraction contrast.

The dislocations (and associated plastic strain) are also observed at the interfaces in larger precipitates (Supplementary Fig. S3d–g). The Burger's circuit around the dislocation core yields a closure failure with a projected vector 1/2 a[011]. We note that high-density misfit dislocations appear in many larger size precipitates in PbTe containing 2% SrTe and 1% Na$_2$Te, suggesting that the density of dislocations is about double the number density of SrTe nanocrystals.

To understand the role of the SrTe nanocrystals in reducing the lattice thermal conductivity, we performed theoretical calculations of the lattice thermal conductivity based on the Callaway model[26]. The lattice thermal conductivity is given by:

$$\kappa_{\mathrm{lat}} = \frac{k_B}{2\pi^2 \upsilon}\left(\frac{k_B T}{\hbar}\right)^3 \left\{ \int_0^{\theta_D/T} \tau_c \frac{x^4 e^x}{(e^x-1)^2}\,\mathrm{d}x \right.$$

$$\left. + \frac{\left[\int_0^{\theta_D/T} \frac{\tau_c}{\tau_N}\frac{x^4 e^x}{(e^x-1)^2}\,\mathrm{d}x\right]^2}{\int_0^{\theta_D/T}\frac{1}{\tau_N}\left(1-\frac{\tau_c}{\tau_N}\right)\frac{x^4 e^x}{(e^x-1)^2}\,\mathrm{d}x} \right\}$$
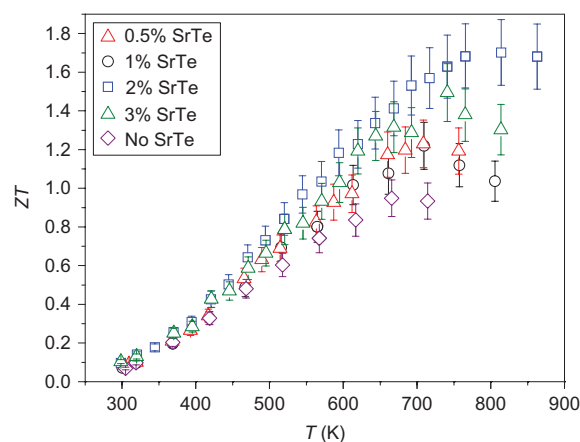

Figure 4 | ZT of PbTe–SrTe. The thermoelectric figure of merit (ZT) as a function of temperature for PbTe–SrTe samples doped with 1% Na$_2$Te. The ZT of a control sample with no SrTe is also shown for comparison. The error bars represent the standard deviation of the mean.

where k_B is the Boltzmann's constant, $\hbar$ is Plank's constant, T and θ_D are respectively the absolute temperature and the Debye temperature, υ is the average phonon-group velocity, $x = \hbar\omega/\kappa_B T$, τ_N is relaxation time due to normal phonon–phonon scattering and τ_c is the combined relaxation time. The latter is obtained by integrating the relaxation times from various processes. Based on TEM studies, for the same frequency, the relaxation time depends mainly on scattering from the nanoscale precipitates, dislocations, boundaries and the phonon–phonon interactions. The overall relaxation time is:

$$\tau_c^{-1} = \tau_U^{-1} + \tau_N^{-1} + \tau_B^{-1} + \tau_S^{-1} + \tau_D^{-1} + \tau_P^{-1}$$

where τ_U, τ_N, τ_B, τ_S, τ_D and τ_P are the relaxation times corresponding to scattering from Umklapp processes, normal processes, boundaries, strains, dislocations and precipitates[27–32]. Based on these formulae and the parameters obtained from the TEM observations (average precipitate size, precipitate density and dislocation density) and from ref. 32, we have calculated the lattice thermal conductivity of PbTe containing 2% SrTe and 1% Na$_2$Te. The results are shown in Fig. 2b and match the experimental data reasonably well although the temperature dependence near room temperature is somewhat weaker than the experimental data. Our calculations indicate that the phonon scattering relaxation time of the endotaxial nanoscale precipitates is shorter than that of the other processes, which means they play a dominant role in reducing the lattice thermal conductivity.

Figure 4 presents the ZT values as a function of temperature for different PbTe–SrTe samples doped with 1% Na$_2$Te. For comparison, we also include ZT data for a control sample containing no SrTe. The highest ZT achieved was 1.7 at 815 K for a 2% SrTe sample. This material maintains the figure of merit above unity over a wide temperature range above 550 K. This SrTe-containing system outperforms other state-of-the-art bulk p-type systems such as TAGS ((AgSbTe$_2$)$_{0.15}$(GeTe)$_{0.85}$, $ZT \approx 1.2$ at 720 K)[33], β-Zn$_4$Sb$_3$ ($ZT \approx 1.3$ at 670 K)[34], AgPb$_m$Sn$_n$SbTe$_{2+m+n}$ ($ZT \approx 1.45$ at 630 K)[11] and NaPb$_m$SbTe$_{2+m}$ ($ZT \approx 1.65$ at 675 K)[12]. Samples containing 0.5% SrTe and 1% SrTe achieved ZT values of ~1.23 at 710 K and ~1.22 at 710 K, respectively (Fig. 4). A sample with 3% SrTe also has a high ZT value of ~1.5 at 750 K, but the mechanical properties were poor. With the increase of SrTe concentration, a shift in the ZT_{max} peak temperature from 710 to 815 K was observed, which is attributed to a slight increase in the band gap of PbTe with the insertion of SrTe.

Conclusions

In summary, we have demonstrated microstructural design with superior thermoelectric properties in bulk p-type PbTe–SrTe through targeted nanostructure/matrix crystallographic alignment that creates endotaxially placed nanoscale precipitates within the matrix, coupled with small electronic band offsets mediated by elastic strain at interfaces. Unlike previous reports of bulk materials, the present case is the first example where the nanostructures do not reduce the power factor; they function exclusively as phonon scattering (microstructural) features to reduce the lattice thermal conductivity, especially at high temperatures. This is an ideal endotaxial nanostructured bulk thermoelectric system—in that it is a genuine phonon-blocking hole transmitting medium—which has also been observed in some epitaxial superlattice thin films[15].

Methods

Synthesis. Ingots (∼10 g) with nominal compositions of PbTe–SrTe (SrTe = 0.5–2 mol%) doped with Na_2Te (1 mol%) were synthesized by mixing appropriate ratios of high-purity Pb, Te, Na_2Te and SrTe in carbon-coated quartz tubes under an argon-filled glove box. The tubes were sealed under high vacuum (∼10^{-4} Torr) and heated to 1,323 K over 15 h and then held there for 10 hours. After that, the samples were slowly cooled to 873 K at a rate of 11 K h^{-1} and then cooled to room temperature over 15 h. Samples were cut and polished in the presence of ethanol for further electrical and thermal conductivity characterization. Samples containing 3% SrTe and 1% Na_2Te were also synthesized, but the mechanical properties of those samples were poor (electrical and thermal transport data of these samples are shown in Supplementary Fig. S4). Control samples containing 1% Na_2Te but no SrTe and 2% SrTe but no Na_2Te have been fabricated by the above mentioned sealed tube reaction with similar heating profile. Electrical and thermal transport data of PbTe containing 2% SrTe is shown in Supplementary Fig. S5.

Powder X-ray diffraction. The powder diffraction patterns were obtained using Cu K_α ($\lambda = 1.5418$ Å) radiation in a reflection geometry on an Inel diffractometer equipped with a position-sensitive detector and operating at 40 kV and 20 mA.

Thermogravimetric analysis. Thermogravimetric analysis was performed using a TGA-50 Shimadzu thermogravimetric analyser under nitrogen in the temperature range 300 to 900 K with a rate of 5 K min^{-1}.

Electrical properties. The electrical conductivity and Seebeck coefficient were measured simultaneously under a helium atmosphere from room temperature to about 850 K on a ULVAC-RIKO ZEM-3 instrument system. Typical samples for measurement had a rectangular shape with the dimensions of ∼2 mm × 3 mm × 8 mm. The longer direction coincides with the direction in which the thermal conductivity was measured. Heating and cooling cycles give repeatable electrical properties for a given sample. Electrical properties obtained from different slices from the same ingot were similar.

Hall measurements. The Hall coefficient was measured with a homemade high temperature apparatus, which provides a working range from 300 to 700 K. The sample was press mounted and protected with argon gas to avoid possible oxidization at high temperature. The Hall resistance was monitored with Linear Research AC Resistance Bridge (LR-700), with constant magnetic fields of ±1 T applied using an Oxford Superconducting Magnet.

Thermal conductivity. Thermal diffusivity, D, was directly measured and heat capacity, C_p, was indirectly derived using a standard sample (pyroceram) in the range 300–850 K using laser flash diffusivity method in a Netzsch LFA-457. Discs with ∼8 mm diameter and ∼2 mm thickness were used in all the measurements. Heating and cooling cycles give repeatable diffusivity for a given sample. Thermal diffusivities obtained for different slices from the same ingot were similar. The total thermal conductivity, κ_{total}, was calculated using the formula, $\kappa_{total} = DC_p\rho$, where ρ is the density of the sample, measured using sample dimension and mass. The sample density was also reconfirmed by gas pycnometer (Micromeritics AccuPyc 1340) measurements.

Transmission electron microscopy. The samples were characterized under the JEOL 2100F TEM. We prepared TEM samples by conventional standard methods. The samples were cut into 3-nm-diameter discs by a disc cutter, then ground, dimpled, polished and subsequently argon-ion milled on a stage cooled with liquid nitrogen.

References

1. Chen, G., Dresselhaus, M. S., Dresselhaus, G., Fleurial, J. P. & Caillat, T. Recent development in thermoelectric materials. *Int. Matter. Rev.* **48,** 45–66 (2003).

2. Rowe, D. M. *CRC Handbook of Thermoelectrics: Macro to Nano* (CRC Press/Taylor & Francis, 2006).

3. Snyder, J. G. & Toberer, E. S. Complex thermoelctric materials. *Nature Mater.* **7,** 105–114 (2008).

4. Sootsman, J., Chung, D. Y. & Kanatzidis, M. G. New and old concepts in thermoelectric materials. *Angew. Chem. Int. Ed.* **48,** 8616–8639 (2009).

5. Heremans, J. P. *et al.* Enhancement of thermoelectric efficiency in PbTe by distortion of the electronic density of states. *Science* **321,** 554–557 (2008).

6. Ahmad, S., Hoang, K. & Mahanti, S. D. *Ab Initio* study of deep defect states in narrow band-gap semiconductors: group III impurities in PbTe. *Phys. Rev. Lett.* **96,** 56403(1–4) (2006).

7. Sootsman, J. R. *et al.* Large enhancement in the power factor of bulk PbTe at high temperature by synergistic nanostructuring. *Angew. Chem. Int. Ed.* **47,** 8618–8622 (2008).

8. Hsu, K. F. *et al.* Cubic $AgPb_mSbTe_{2+m}$: bulk thermoelectric materials with high figure of merit. *Science* **303,** 818–821 (2004).

9. Quarez, E. *et al.* Nanostructuring, compositional fluctuations, and atomic ordering in the thermoelectric materials $AgPb_mSbTe_{2+m}$. The myth of solid solutions. *J. Am. Chem. Soc.* **127,** 9177–9190 (2005).

10. Zhou, M., Li, J.-F. & Kita, T. Nanostructured $AgPb_mSbTe_{2+m}$ system bulk materials with enhanced thermoelectric performance. *J. Am. Chem. Soc.* **130,** 4527–4532 (2008).

11. Androulakis, J. *et al.* Nanostructuring and high thermoelectric efficiency in p-type $Ag(Pb_{1-y}Sn_y)_mSbTe_{2+m}$. *Adv. Mater.* **18,** 1170–1173 (2006).

12. Poudeu, P. F. P. *et al.* High thermoelectric figure of merit and nanostructuring in bulk p-type $Na_{1-x}Pb_mSb_yTe_{2+m}$. *Angew. Chem. Int. Ed.* **45,** 3835–3839 (2006).

13. Androulakis, J. *et al.* Spinoidal decomposition and nucleation and growth as a means to bulk nanostructured thermoelectric: enhanced performance in $Pb_{1-x}Sn_xTe\_PbS$. *J. Am. Chem. Soc.* **129,** 9780–9788 (2007).

14. Poudel, B. *et al.* High-thermoelectric performance of nanostructured bismuth antimony telluride bulk alloys. *Science* **320,** 634–638 (2008).

15. Venkatasubramanian, R., Siivola, E., Colpitts, V. & O'Quinn, B. Thin-film thermoelectric devices with high room-temperature figures of merit. *Nature* **413,** 597–602 (2001).

16. Slack, G. A. New materials and performance limits for thermoelectric cooling. In *CRC Hand Book of Thermoelectrics* (Ed. D. M. Rowe), 407–440 (CRC Press, Boca Raton, 1995).

17. Allgaier, R. S. & Houston, B. B. Jr. Hall coefficient behavior and second valence band in lead telluride. *J. Appl. Phys.* **37,** 302–309 (1966).

18. Ravich, Y. I., Efimova, B. A. & Smirnov, I. A. *Semiconducting Lead Chalcogenides* (Plenum, New York, vol. 5, 1970).

19. Crocker, A. J. & Rogers, L. M. Valence band structure of PbTe. *J. Phys. Colloques* **29,** C4-129–C4–132 (1968).

20. Dawar, A. L., Taneja, O. P., Paradkar, S. K., Kumar, P. & Mathur, P. C. Electrical transport properties of thallium-doped p-type PbTe films. *Thin Solid Films* **78,** 153–159 (1981).

21. Varshni, Y. P. Temperature dependence of the energy gap in semiconductors. *Physica* **34,** 149–154 (1967).

22. Rogers, L. M. The Hall mobility and thermoelectric power of p-type lead telluride. *Brit. J. Appl. Phys.* **18,** 1227–1235 (1967).

23. Vineis, C. J. *et al.* Carrier concentration and temperature dependence of the electronic transport properties of epitaxial PbTe and PbTe/PbSe nanodot superlattice. *Phys. Rev. B* **77,** 235202-1-14 (2008).

24. Partin, D. L., Thrush, C. M. & Clemens, B. M. Lead strontium telluride and lead barium telluride grown by molecular-beam epitaxy. *J. Vac. Sci. Technol. B* **5,** 686–689 (1987).

25. Hytch, M. J., Snoeck, E. & Kilaas, R. Quantitative measurement of displacement and strain fields from HREM micrographs. *Ultramicroscopy* **74,** 131–146 (1998).

26. Callaway, J. & Von Baeyer, H. C. Effect of point imperfections on lattice thermal conductivity. *Phys. Rev.* **120,** 1149–1154 (1960).

27. Morelli, D. T. & Heremans, J. P. Estimation of the isotope effect on the lattice thermal conductivity of group IV and group III-V semiconductors. *Phys. Rev. B* **66,** 195304 (2002).

28. Chen, G., Dames, C., Song, D. & Harris, C. T. in *Thermal conductivity 27/thermal expansion 15* (Eds. Huang, H. & Porter, W.) 263–269 (DEStech Publication, 2004).

29. Chen, G., Zeng, T., Borca-Tascius, T. & Song, D. Phonon engineering in nanostructures for solid-state energy conversion. *Mat. Sci. Eng. A* **292,** 155–161 (2000).

30. Kim, W. & Majumdar, A. Phonon scattering cross section of polydispersed spherical nanoparticles. *J. Appl. Phys.* **99,** 084306 (2006).

31. Mingo, N., Hauser, D., Kobayashi, N. P., Plissonnier, M. & Shakouri, A. 'Nanoparticle-in-Alloy' approach to efficient thermoelectrics: silicides in SiGe. *Nano Letters* **9,** 711–715 (2009).

32. He, J. Q., Girard, S. N., Kanatzidis, M. G. & Dravid, V. P. Microstructure-lattice thermal conductivity correlation in nanostructured $PbTe_{0.7}S_{0.3}$ thermoelectric material. *Adv. Fun. Mater* **20,** 764–772 (2010).

33. Wood, C. Materials for thermoelectric energy conversion. *Rep. Prog. Phys.* **51,** 459–539 (1988).

34. Snyder, G. J., Christensen, M., Nishibori, E., Caillat, T. & Iversen, B. B. Disordered zinc in Zn_4Sb_3 with phonon-glass and electron-crystal thermoelectric properties. *Nature Mater.* **3,** 458–463 (2004).

Author contributions

K.B., Q.Z. and M.G.K. prepared the samples, designed and carried out thermoelectric experiments. K.B. and M.G.K. analysed the electrical and thermal transport data. J.H. and V.P.D. carried out the TEM experiment and analysed the TEM data. G.W. and C.U. carried out the Hall measurements. K.B., J.H., V.P.D. and M.G.K. wrote the manuscript. All authors have reviewed, discussed and approved the results and conclusions of this article.

Additional information

The authors declare no competing financial interests. Supplementary information accompanies this paper at www.nature.com/naturechemistry. Reprints and permission information is available online at http://npg.nature.com/reprintsandpermissions/. Correspondence and requests for materials should be addressed to M.G.K.